PAPER

Check for updates

Highly efficient broadband photodetectors based on lithography-free Au/Bi$_2$O$_2$Se/Au heterostructures†

Xiaolong Liu,[a] Ruiping Li,[b] Chengyun Hong,[a] Gangfeng Huang,[a] Danfeng Pan,*[c] Zhenhua Ni,[d] Yongqing Huang,[e] Xiaomin Ren,[e] Yingchun Cheng ◉ *[b] and Wei Huang[b,f]

As one of the bismuth-based oxychalcogenide materials, Bi$_2$O$_2$Se ultrathin films have received intense research interest due to their high carrier mobility, narrow bandgaps, ultrafast intrinsic photoresponse and long-term ambient stability; they exhibit great potential in electronic and optoelectronic applications. However, the device performance of photodetectors based on metal/Bi$_2$O$_2$Se/metal structures has degraded due to the undesirable defects or contaminants from the electrode deposition or the sample transfer processes. In this work, highly efficient photodetectors based on Au/Bi$_2$O$_2$Se junctions were achieved with Au electrodes transferred under the assistance of a probe tip to avoid contaminants from traditional lighography methods. Furthermore, to improve the charge transfer efficiency, specifically by increasing the intensity of the electrical field at the Au/Bi$_2$O$_2$Se interface and along the Bi$_2$O$_2$Se channels, the device annealing temperature was optimized to narrow the van der Waals gap at the Au/Bi$_2$O$_2$Se interface and the device channel length was shortened to improve the overall device performance. Among all the devices, the maximum device photoresponsivity was 9.1 A W^{-1}, and the device response time could approach 36 μs; moreover, the photodetectors featured broadband spectral responses from 360 nm to 1090 nm.

1 Introduction

Metal/semiconductor/metal (MSM) structures are important in the areas of electronics,[1] optoelectronics,[2] spintronics,[3] gas sensors,[4] *etc*. In these applications, the metal/semiconductor interfaces play important roles, together with the selection of the metal/semiconductor material to tailor the device functions. With the rapid development of the ultrathin material "armory" (with thicknesses down to atomic layer), research on MSM structures has greatly broadened. Among these, Pd/graphene/Ti,[5] Au/MoS$_2$,[6] gate-tunable Co/black phosphorus,[7] Cr/Bi$_2$Se$_3$[8] and numerous other MSM architectures have been explored for application in 1.55 μm optical communications, LEDs, spin valves, infrared photodetectors, *etc*. Photodetectors containing graphene as electrode contacts can be highly efficient due to their atomically flat interfaces with 2D materials and decreased trapping states to avoid Fermi level pinning effects.[9,10] Additionally, the device performance can be modulated with electrical gating on the graphene electrodes,[11,12] demonstrating versatile device functions.[13] High carrier mobility-endowed ultrathin materials maybe useful in high-demand electronics,[14,15] while materials with favorable energy bandgaps can be considered in optoelectronic applications.[16,17] Satisfying these prerequisites, ultrathin Bi$_2$O$_2$Se films are emerging as new Bi-based oxychalcogenide materials[18] that exhibit high carrier mobility due to their small electron effective masses, air-stable features, sub-1 μm bandgaps,[19] and defect-tolerant energy band structures.[20,21] With these outstanding intrinsic physical characteristics, Bi$_2$O$_2$Se

[a] *State Key Laboratory of Alternate Electrical Power System with Renewable Energy Sources and Beijing Key Laboratory of Energy Safety and Clean Utilization, Renewable Energy School, North China Electric Power University, Beijing 102206, China*
[b] *Key Laboratory of Flexible Electronics & Institute of Advanced Materials, Jiangsu National Synergetic Innovation Center for Advanced Materials, Nanjing Tech University, 30 South Puzhu Road, Nanjing 211816, China. E-mail: iamyccheng@njtech.edu.cn*
[c] *National Laboratory of Solid State Microstructures, School of Electronic Science and Engineering Collaborative Innovation Center of Advanced Microstructures, Nanjing University, Nanjing 210093, China. E-mail: pdf@nju.edu.cn*
[d] *Department of Physics, Southeast University, Nanjing 211189, China*
[e] *State Key Laboratory of Information Photonics and Optical Communications, Beijing University of Posts and Telecommunications, Beijing 100876, China*
[f] *Shaanxi Institute of Flexible Electronics (SIFE), Northwestern Polytechnical University, 127 West Youyi Road, Xi'an, 710072, China*
†Electronic supplementary information (ESI) available. See DOI: 10.1039/c9nr06723j

ultrathin films are desirable material choices for MSM structured opto-electronics, together with graphene, transition metal dichalcogenides (TMDs), black phosphorus, etc.

For photodetection applications, although the intrinsic photo-response times at the metal/Bi_2O_2Se junction are in the order of picoseconds,[22] the device response speeds of the as-fabricated photodetectors on mica are about a millisecond,[23] while those of the photodetectors fabricated on SiO_2/Si substrates are several hundred μs.[24] From this point of view, the bandwidth of metal/Bi_2O_2Se structures is far from well explored, prohibiting further application of Bi_2O_2Se-based photodetectors. In planar MSM structures, the limited device bandwidth is mainly attributed to inefficient photo-induced carrier separation and collection routes or the accumulation of defects or trapping states at the metal/semiconductor interface during the electrode deposition process,[25] which are inevitable in traditional lithography techniques (ultraviolet lithography or electron beam lithography). The disadvantages of the device fabrication process represent an overwhelming problem for photoelectronic devices based on ultrathin materials because the quality of the interfaces between the metals, semiconductors and substrates can apparently affect the device performance.

Specifically, the bombardment of the metal elements during deposition procedures causes glassy morphologies or physical damage to the active layers. As a result, intrinsic Schottky-type contact formation is prohibited, i.e., the Fermi level pinning effect prevails at the metal/semiconductor interfaces.[26–28] Consequently, modulation of the energy band alignment in MSM structures by empirically adopting metals with different work functions is prone to frustration. To solve these problems, novel electrode fabrication techniques have been explored, and two-dimensional metallic materials were investigated to form van der Waals-type metal–semiconductor contacts. Among these, adhesive polymer-assisted electrode transfer was achieved to approach the Schottky–Mott limit with the metal selection, adjusting n- or p-typed efficient carrier transport in MoS_2 field effect transistors (FETs).[25] The graphene electrodes transferred on the two-layer-thick organic FETs effectively lowered the contact resistance.[29] Innovatively, an ultralow contact resistance, 0.5 kΩ μm, was obtained for the epitaxial lateral metal–semiconductor heterostructures of VS_2/MoS_2.[30]

In this work, in-plane Au/Bi_2O_2Se/Au MSM structures were fabricated on fluorophlogopite mica (abbreviated as f-mica) substrates to form metal/semiconductor contacts. The electrode fabrication process was achieved with a probe tip under an optical microscope to transfer the as-deposited pre-patterned Au electrodes onto the Bi_2O_2Se films. Additionally, the 2D material transfer process generally introduces unfavorable gas bubbles or oxygen–water adhesives at the semiconductor/substrate interfaces.[31] Bi_2O_2Se thin films are transferred onto SiO_2/Si substrates by polymer-assisted peeling of the samples followed by the dissolution of the residual glue, which maybe the reason for the decreased device speed.[24] Herein, freshly cleaved f-mica flakes were used as substrates

for Bi_2O_2Se thin film growth; although the electrical gating-associated photo-induced carrier multiplication was sacrificed, the additional traps during the sample transfer process were avoided. In this way, the interfaces at the Au/Bi_2O_2Se and Bi_2O_2Se/substrate were pristine, without contaminants or damages from the traditional electrode deposition and film transfer processes. Highly efficient photodetectors were then fabricated; with the optimized annealing temperature and channel length, the maximum photo-responsivity was 9.1 A W^{-1}, the device response speed could be as fast as 36 μs, and broadband spectral response was demonstrated from the ultraviolet to near infrared region.

2 Results and discussion

2.1 Au/Bi_2O_2Se/auphotodetectors

The growth of the Bi_2O_2Se thin films was carried out in a home-built quartz tube furnace using Bi_2O_3 and Bi_2Se_3 as the precursor powders and freshly cleaved f-mica as the growth substrate placed downstream in N_2 as the carrier gas (as illustrated in Fig. 1a). The as-grown Bi_2O_2Se thin films exhibited square morphologies in the optical microscopy images in Fig. 1b, which is the prevailing appearance at relatively high growth temperatures.[18,23] The Bi_2O_2Se films follow the I4/mmm group symmetry, with $[Bi_2O_2]^{2+}$ and Se^{2-} layers repeated alternatively with weak electrostatic intra-layer interactions.[20,21] The crystal structure of the Bi_2O_2Se film is schematically illustrated in Fig. S1.† Furthermore, Raman characterization was performed on the Bi_2O_2Se samples, in which the typical A_{1g} peak at around 161 cm^{-1} of the Bi_2O_2Se on f-mica can be observed.[32]

Based on the as-grown Bi_2O_2Se thin films, the Au/Bi_2O_2Se/Au MSM structures were fabricated by transferring the Au electrodes from the SiO_2/Si substrates onto the Bi_2O_2Se films with the assistance of a probe tip, as depicted in the schematic in Fig. 1d. In this way, the interfaces between the Au electrodes and the Bi_2O_2Se films were pristine, and contaminants or defects from the traditional lithography-assisted electrode fabrication processes were avoided. The AFM images in Fig. S2† further prove that the electrical conducting channels of Bi_2O_2Se were clean from lithographic organic residues.

However, the intrinsic electrical transporting behavior in the Au/Bi_2O_2Se/Au MSM structures was unsatisfactory. As shown in Fig. S3,† the current was at the pA scale and unfavorable electrical noise was observed in the output curves; this can be attributed to the large van der Waals gap between the Au electrodes and Bi_2O_2Se, resulting in poor metal/semiconductor contacts.[26,33] Additionally, the photoresponsivity R, defined as I_{ph}/P, was 0.6 A W^{-1}, where I_{ph} is the photocurrent and P is the incident laser power on the Bi_2O_2Se light absorbing area.

To achieve better metal/semiconductor contacts, the Au/Bi_2O_2Se/Au devices were annealed in vacuum conditions at an optimized temperature of 120 °C to eliminate adhesive water/oxygen at the MSM interfaces; this can narrow the van der Waals gap through closer metal/semiconductor contacts. As a
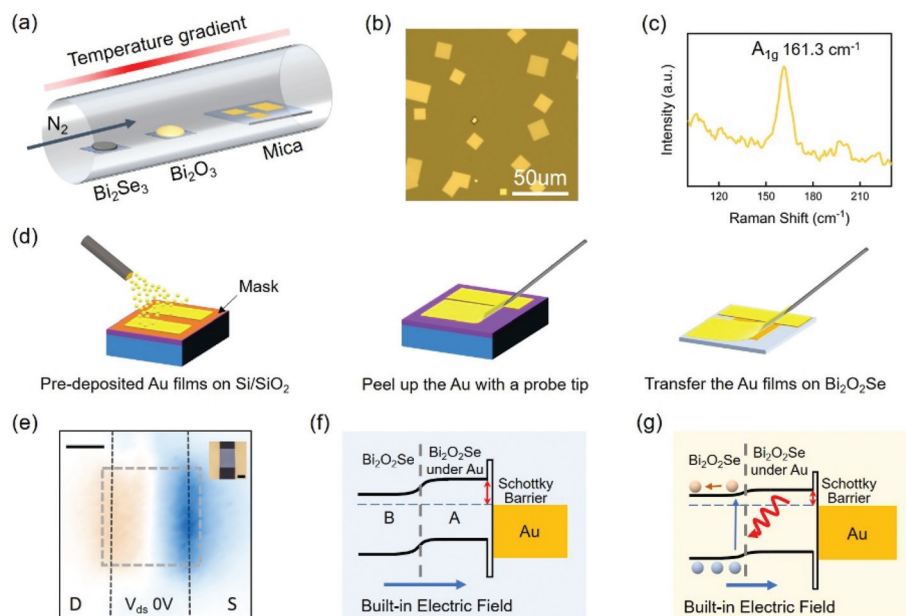
Fig. 1   The growth of the Bi_2O_2Se film and the $Au/Bi_2O_2Se/Au$ structure fabrication. (a) Schematic of the growth of the Bi_2O_2Se thin films with the chemical vapor deposition method. (b) Optical microscopic image of the as-grown Bi_2O_2Se thin films with square morphologies on *f*-mica. (c) The Raman characterization of the as-grown Bi_2O_2Se sample. (d) Schematic of the probe tip-assisted Au electrode fabrication process. (e) The photocurrent mapping of the $Au/Bi_2O_2Se/Au$ structure on the *f*-mica substrates; the optical image of the device is in the inset. The scale bar is 5 μm. The region in blue denotes negative I_{ph}, while orange is positive I_{ph}. The square dash line outlines the Bi_2O_2Se sample. (f) The energy band diagram of the Au/Bi_2O_2Se heterostructure with the Schottky barrier formed at the interfaces. (g) The energy band diagram of the Au/Bi_2O_2Se structure under illumination.

result, both the electrical and optoelectronic properties of the devices were effectively improved (which will be described in detail in the following sections). It should be mentioned that the Au electrodes could still be peeled up without damaging the Bi_2O_2Se films, as shown in the optical image in Fig. S2b;† also, from the AFM characterizations in Fig. S2h,† the regions under the Au electrodes remained contaminant-free. A similar phenomenon was reported in a polymer-assisted electrode transfer process on MoS_2 films.[25]

2.2   Device performance

The photocurrent mapping of the annealed devices was performed under a 50× objective lens with 640 nm laser illumination; the laser spot was about 1 μm, and the voltage bias was firstly set as 0 V. The electrodes were marked as "source" and "drain" for convenience. From the mapping results in Fig. 1e, the areas near the metal/Bi_2O_2Se contact edges were the most effective photo-electric conversion regions with the largest photocurrents. However, some of the Au electrodes also exhibited photo-response, which can be explained by the fact that the laser spot covered both the electrodes and the active regions. An optical image of the corresponding device is shown in the inset of Fig. 1e. Correspondingly, the device working mechanism is illustrated in the energy band diagrams in Fig. 1f and g, and the relative location between the energy band edges of Bi_2O_2Se and the working function of Au was obtained from the first principles calculations described in the ESI.† The n-type Fermi level located in the Bi_2O_2Se energy

band was confirmed by published work;[18] additionally, the transfer curve of the Bi_2O_2Se FET based on the Bi_2O_2Se film transferred from mica onto the SiO_2/Si substrates is demonstrated in Fig. S4,† indicating the n-type carrier transport. For convenience, the Bi_2O_2Se under the Au electrodes is labelled as region A, while the Bi_2O_2Se away from the electrodes is region B. The Fermi level of region A remains the same with the Au working function; then, a homojunction forms readily along with the carrier depletion between region A and B. When the incident light is absorbed, the electron–hole pairs can be separated under the built-in electrical field along the Bi_2O_2Se lateral junctions, followed by collection of the photoinduced carriers by the Au electrodes, as shown in Fig. 1g. With the drain electrode grounded, holes drifted under the electrical field pointing from region B to region A; then, the sign of the photocurrent was positive near the drain electrode and negative at the source electrode edge, which is proved in the photocurrent (abbreviated as I_{ph}) mapping results in Fig. 1e and further confirmed in Fig. 2 by the non-zero voltage bias. The I_{ph} mapping with the intensity scale is in Fig. S5† corresponding to Fig. 1e; besides that, the full-scale optical image and the AFM characterization of the device are included in Fig. S5.†

Considering that the electrodes were fabricated "manually", the symmetry of the electrodes should be explored; this was testified by the photocurrent mapping results under different voltage biases. In Fig. 2a, at a small positive voltage bias of 10 mV, the positive I_{ph} region near the drain electrode expanded, although the negative I_{ph} region shrank correspondingly.
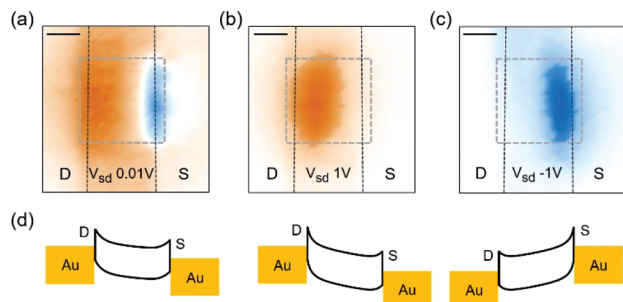
Fig. 2 The photocurrent mapping results of the Au/Bi$_2$O$_2$Se/Au photodetector and the corresponding energy band structures under different voltage biases. (a) The photocurrent mapping at $V_{sd} = 0$ V. The orange region denotes positive I_{ph}, while the blue region is negative. The scale bar is 5 μm. (b) The photocurrent mapping at $V_{sd} = 1$ V. The dominant positive photoresponse takes place near the drain electrode. (c) The photocurrent mapping at $V_{sd} = -1$ V. The dominant negative photoresponse is near the source electrode. (d) The energy band diagrams to explain the I_{ph} mapping results from (a) to (c).

Fig. 3 Device performance of the Au/Bi$_2$O$_2$Se/Au photodetectors. (a) The photoresponse increases with the laser power density. (b) The dependence of I_{ph} on the laser power density. The blue scattered dots are the experimental results, and the red line is the fitting results with $I_{ph} = P^{0.94}$. (c) Spectral response under illumination with different photon wavelengths; the light power was fitted as 0.5 nW in the light absorbing region defined by the electrodes. (d) Photocurrent under on/off modulation of a 640 nm laser. (e) The exponential fitting of the normalized I_{ph} rising edge from the enlarged curve in Fig. S9b;† the response time is 47.6 μs. (f) The exponential fitting of the normalized I_{ph} decay edge from Fig. S9b;† the carrier lifetime is 32.5 μs.

At a larger positive voltage of 1 V, the above trend was more obvious, while at a negative voltage of −1 V, the trend was reversed. Comparing Fig. 2b and c, at the same absolute voltage bias, the negative effective region was smaller than the positive region, which can be attributed to the subtle difference between the two electrodes from the aspects of contact area, contact quality, electrode edge roughness, *etc.* The corresponding energy band diagram is drawn in the lower panel of Fig. 2; it clearly explains the I_{ph} mapping results, where the voltages with different signs can either strengthen or weaken the electrical fields near different electrodes. The I_{ph} mapping images with intensity scale are shown in Fig. S6.†

The device performance was further measured under a 640 nm laser with different power densities, as shown in Fig. 3a. The laser spot was of 1 cm^2 to cover the whole active region in the MSM structures. The light-to-dark current ratio between the current at 5 mW cm^{-2} laser power and that in dark conditions approached 10^2. The full scale dark current curve was plotted in both linear and logarithmic coordinates, as shown in Fig. S7.† In Fig. 3b, the dependence of I_{ph} on the incident laser power P could be fitted by the relation of $I_{ph} = A \times P^\alpha$, where A and α are the fitting parameters. Here, A equals 1, and from the best fitting results, α is 0.94; this is close to unity and reflects that the photocurrent increased almost linearly with the incident light, while trapping, recombination and other unfavorable mechanisms were suppressed in the MSM structures.[34,35] The maximum photoresponsivity R was 1 A W^{-1} at the laser power of 1 mW cm^{-2}. Furthermore, the spectral response of the fabricated device could extend from 360 nm to 1090 nm, as shown in Fig. 3c; the weak response region from 800 nm is magnified in the inset with the corresponding $I_{ph} \sim \lambda$ curve in Fig. S8.† The peak in the spectral response curve was at 470 nm, which varied from the micro-optical results of the Bi$_2$O$_2$Se films at the maximum absorption of 450 nm;[32] this can be attributed to the energy structure changes caused by the different sample growth con-
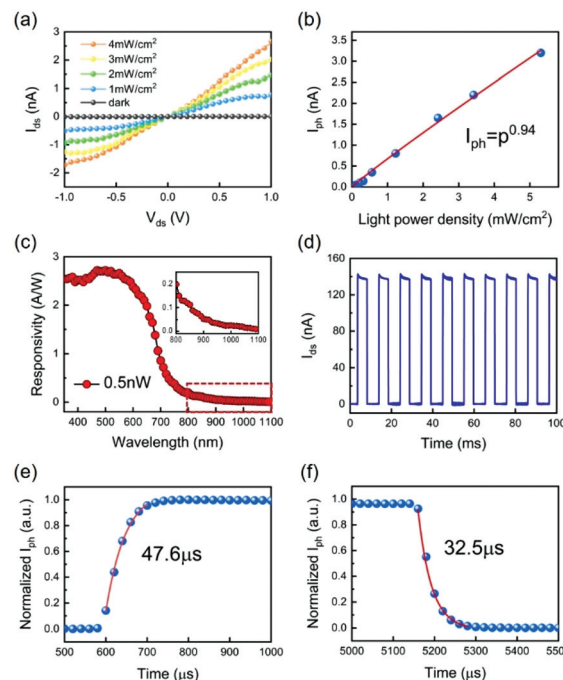
ditions.[20] The incident light power for the spectral response measurement was fixed as 0.5 nW at different wavelengths. It should be mentioned that the thickness of the Bi$_2$O$_2$Se film for the opto-electric measurements in Fig. 3 was 9.8 nm from the AFM results in Fig. S5c,† which is about 16 layers considering that the thickness of the Bi$_2$O$_2$Se monolayer was 6.08 Å; thus, it could be treated as bulk Bi$_2$O$_2$Se both for the optical absorption measurements[32] and the energy band structure calculations.[20,21] Considering that the Bi$_2$O$_2$Se films have a bandgap of about 0.8 eV from the angle-resolved photoemission spectroscopy results (1553 nm photon absorption, alternatively),[22] the response spectrum could be broadened even further with the amplified weak I_{ph} signal at longer wavelengths employing photo-induced carrier multiplication effects with electrical gate voltage modulation or by combining the MSM structures with other light-absorbing materials.[36,37]

The device response speed is an important opto-electronic figure of merit for photodetectors; it was characterized with the device dynamic photocurrent response under on/off modulation of a laser, as shown in Fig. 3d. From the enlarged curves, the rising and decay edges of the photocurrent were fitted with the single exponential functions of

$I = I_{\text{dark}} + A \exp((t - t_0)/\tau_{\text{rise}})$ and $I = I_0 \exp((-(t - t_0))/\tau_{\text{decay}})$, respectively, where I_{dark} is the dark current (set as zero), t_0 is the time label when the current begins to grow under light illumination or to decay after turning off the laser, A and I_0 are the fitting parameters (specifically, I_0 is the saturated photocurrent), τ_{rise} is the I_{ph} rising lifetime, fitted as about 47.6 μs in Fig. 3e, and τ_{decay} is the trailing (recombination) lifetime of about 32.5 μs, as shown in Fig. 3f. Although there were spikes in the rising edges of the I_{ph} time-sampling curve in Fig. 3d, from the enlarged individual modulated photocurrent curve demonstrated in Fig. S9,† the rising edge fitting was not influenced. The relatively slower τ_{rise} lifetime compared with τ_{decay} can be explained by the insufficient electrical field intensity along the Bi_2O_2Se homojunction originating from the difference between the Au work function and the Bi_2O_2Se fermi level. Although the response speed was far from the intrinsic picosecond lifetime at the metal/Bi_2O_2Se junctions,[22] this device was among the fastest compared with other thin film-based MSM-structured photodetectors.[23,34,38] The improved device bandwidth arises from the fact that high-quality metal/semiconductor junctions were achieved with the probe-tip-assisted Au electrode transfer. Additionally, the unfavorable defect and trap center concentrations were decreased by avoiding the transfer process of Bi_2O_2Se films from f-mica to other substrates; accordingly, contaminants from the adhesive polymer and organic solvent were also prevented. To further accelerate the device response (and to improve the quantum efficiency at the same time), metals with lower work functions, such as Pd or Pt, should be adopted; this can strengthen the electrical field along the Bi_2O_2Se homojunction with increased Schottky barriers at the metal/Bi_2O_2Se interfaces. Furthermore, the intrinsic Se vacancy density in the Bi_2O_2Se film should be modulated by carefully tuning the precursor evaporation speed and other growth parameters.[20]

2.3   Device performance improvement

To further improve the overall device performance, the photocurrent mapping patterns in Fig. 2b and c were analysed in-depth. From these, the active region was dominantly located near the electrode edges under bias, and the photo-electric conversion on the area away from the working regions was unexploited; this is attributed to the insufficient carrier depletion length or weak lateral internal electrical field. To solve this problem, a device with narrow channel length of about 0.8 μm was fabricated (optical microscopic images of the device are shown in the insets of Fig. 4a and Fig. S10a;† the AFM results are shown in Fig. S10b,† and the film thickness was 8.1 nm, as measured in Fig. S10c†), within which both the internal and external electrical field could enhance the photo-induced electron–hole pair separation and collection along the entire Bi_2O_2Se channel area. In this way, the photo-carrier transfer efficiency could be effectively improved.

From the photocurrent mapping results in Fig. 4a, it is obvious that under a voltage bias with a positive or negative sign, the light absorbing region was fully utilized; this denotes high external quantum efficiency, which is defined as the
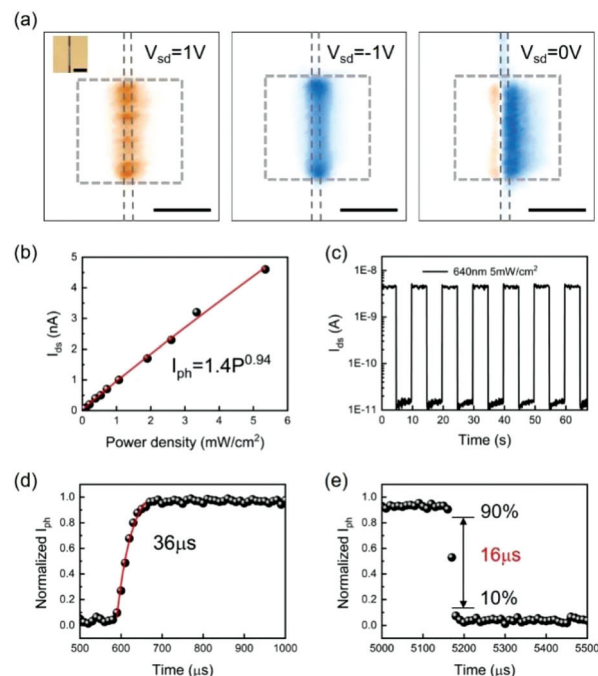

Fig. 4 The photocurrent mapping of the Au/Bi_2O_2Se/Au photodetector with 0.8 μm channel length and the performance of the device. (a) With the short Bi_2O_2Se channel, the electrical field covers the whole light absorbing area; correspondingly, the quantum efficiency is improved. The sign of I_{ph} under different voltage biases is the same as the results in Fig. 2. The scale bar is 10 μm. (b) The fitting of the $I_{\text{ph}} - P$ dependence with $I_{\text{ph}} = 1.4P^{0.94}$. The black dots are the experimental data and the red line is the fitting curve. (c) Logarithmic plot of the dynamic photocurrent response modulated by turning the 640 nm laser on and off. (d) The response time of the Au/Bi_2O_2Se/Au photodetector with a short channel was accelerated to 36 μs with single exponential fitting. (e) The 16 μs lifetime at the falling edge of I_{ph} was abstracted with the 10% to 90% method.

photo-induced carriers collected compared with the number of incident photons in the light-absorbing area. The I_{ph} mapping results with intensity scale are included in Fig. S11.† The dependence of I_{ph} on the laser power density in Fig. 4b could also be fitted as $I_{\text{ph}} = A \times P^{\alpha}$, where A equals 1.5 and α is 0.94; this reflects the linear dependence of I_{ph} on the laser power, which is shown in Fig. 3. The maximum responsivity could approach 6 A W^{-1}, with an enhanced EQE of 1165%. The over-100% EQE arises from the multiplication effect induced by the trapped photo-induced carriers in the annealed Bi_2O_2Se films or at the Au/Bi_2O_2Se interfaces. The detectivity (D^*) equals 1.3×10^8 Jones; this was calculated as $D^* = RS^{1/2}/(2eI_{\text{dark}})^{1/2}$, where S is the device area (15.7 μm^2), e is the element charge and I_{dark} is the dark current (10^{-11} A). Furthermore, because the device with a narrow channel could effectively promote the processes of photo-induced carrier separation, diffusion and collection, the device response speed was accelerated with a τ_{rise} of 36 μs, and an even faster lifetime in the decay edge of 16 μs was abstracted from the 10% to 90% method when considering the measurement limitation. The device response is limited by the slow opto-electronic process; thus, here, 36 μs rather than

16 μs should be the characteristic response speed of the device. Photoresponse enhancement with shrinking electrode spacing was also observed in GaSe-based photodetectors.[39]

Finally, the influence of the annealing temperature on the device performance was explored at a higher temperature of 200 °C; as shown in Fig. 3, the device had been annealed under 120 °C for 1 hour already. It was found that both the dark current and I_{ph} increased (Fig. S12†), which can be explained by the fact that the conducting channel in Bi_2O_2Se was in the $[Bi_2O_2]^{2+}$ layer,[20,21] and the elevated annealing temperature would realize a closer proximity of the electrodes to the $[Bi_2O_2]^{2+}$ layers. Consequently, the device responsivity was increased to 9.1 A W^{-1} (with the EQE improved to 1767%); however, the device obviously decelerated, with I_{ph} rising and falling lifetimes of about 548 μs and 174 μs, respectively (Fig. S12c†), which is one order of magnitude slower than the 120 °C-annealed conditions. This can be attributed to undesirable defect formation during the annealing process at a higher temperature. Peeling up of the electrodes was also performed, as shown in Fig. S2c and S2d,† and it was found from the AFM results that the Bi_2O_2Se film was undamaged. However, the invisible chemical bonding at the metal/semiconductor interfaces or glassy states in the Bi_2O_2Se films may have been generated under 200 °C annealing, considering the slower response speed and the larger-than-unity EQE increase accompanied with the magnified photo-induced carrier multiplication effect. In Table S1,† a device performance comparison between the $Au/Bi_2O_2Se/Au$ photodetectors and previously published Bi_2O_2Se photodetectors is shown, which indicates that the responsivity and response speed of the devices in this work have apparently improved compared with devices on mica; this manifests the advantages of the device fabrication process and the optimized performance conditions.

3   Experimental

3.1   Synthesis of Bi_2O_2Se thin films

The Bi_2O_2Se thin films were grown in a home-built quartz tube furnace. The Bi_2O_3 powder precursor (purchased from Alfa Aesar, with the purity of 99.99%) with a higher evaporation temperature was placed at the center of the heating zone, while Bi_2Se_3 powder (purity of 99.999%, Alfa Aesar) with a relatively low evaporation temperature was placed 8 cm upstream. Fluorophlogopite mica substrates, $KMg_3(AlSi_3O_{10})F_2$, were freshly cleaved and placed in the low temperature deposition zone, 10 cm downstream from the heating center. Nitrogen was used as the carrier gas to assist the Bi_2Se_3 migration, and the flux was 150 sccm. The growth temperature was set as 580 °C for 60 min, after which the furnace was cooled naturally to cease the Bi_2O_2Se film growth. The pressure in the furnace was 2500 Pa as measured by a resistance gauge at the outlet of the quartz tube.

3.2 Bi_2O_2Se sample characterizations

The morphologies of the as-grown Bi_2O_2Se thin films were characterized by optical microscopy (Olympus BX46F). The

thickness and surface cleanliness were measured using an atomic force microscope (Park XE7) in tapping mode. The Raman information was collected using a Princeton ACTON SP2556 spectrometer (1200 G mm^{-1} ruled grating) with a confocal microscope system equipped with a 100× objective lens and 532 nm continuous wave monochromatic laser.

3.3   Device fabrication and optoelectrical measurements

The Au film with a thickness of 100 nm was evaporated on the SiO_2/Si substrates, which were patterned with the TEM grids as the masks. The Au electrodes were then peeled up, then placed on the Bi_2O_2Se films with a probe tip under the optical microscope. In this way, the bottom surface of the Au electrodes duplicated the flatness of the SiO_2/Si surface, and the interface at Au/Bi_2O_2Se was pristine. All the electrical and optoelectrical measurements were performed in a Lakeshore TTPX vacuum probe station under 10^{-3} Pa at room temperature. The I–V curves were obtained with the Agilent B1500 SMU modules. A 500 W xenon lamp with a Zolix Omni-λ200i monochromator was used for the spectral response measurements of the device. The photocurrent measurement under different laser powers was performed under a 640 nm monochromatic laser (a product of Beijing Lasewave Optoelectronics Technology Co. Ltd.) attenuated with the circuit current. The spot size of the incident light (both the 640 nm laser and the light from the 500 W xenon lamp though a monochromator) was 1 cm^2 through the optical aperture for the photoresponsivity and spectral response measurements to cover the whole light absorbing area. During the I_{ph} mapping test, the 640 nm laser was converged through a 50× objective lens; the spot size was 1 μm in diameter. The photocurrent mapping was performed with the Metatest ScanPro system scanning in a line-by-line mode on the piezoelectric stage. The device dynamic response was measured with an NI PCIe-6321 data acquisition card, which also acted as the oscilloscope. The photocurrent curves were the average of 100 times synchronized with the laser modulation.

4.   Conclusions

To summarize, it was demonstrated that by using a lithography-free electrode fabrication process and avoiding the sample transfer procedure, the interfaces at $Au/Bi_2O_2Se/Au$ heterostructures could be contaminant-free, and the defect or trapping centers were effectively decreased. Furthermore, the annealing temperature was optimized to achieve close van der Waals metal/semiconductor contacts; additionally, the device channel length was shortened to make full use of the internal and external electrical fields crossing the entire light absorption region. Highly efficient photodetectors were then constructed with high photoresponsivity, good quantum efficiency and fast response speed. Furthermore, the device featured broadband spectral response from 360 nm to 1090 nm. The application potential of the photodetectors based on the Bi_2O_2Se thin films could be further explored with electrodes

with lower work functions or by interfacing Bi_2O_2Se with other materials to form p–n or p–i–n junctions.

Conflicts of interest

The authors declare no conflicts of interest.

Acknowledgements

Notes and references

1 J. Xia, G. Dong, B. Tian, Q. Yan, H. Zhang, X. Liang and L. Peng, *Nanoscale*, 2016, **8**, 9988–9996.
2 C. K. Wang, S. J. Chang, Y. K. Su, Y. Z. Chiou, S. C. Chen, C. S. Chang, T. K. Lin, H. L. Liu and J. J. Tang, *IEEE Trans. Electron Devices*, 2006, **53**, 38–42.
3 L. Šmejkal, Y. Mokrousov, B. Yan and A. H. MacDonald, *Nat. Phys.*, 2018, **14**, 242–251.
4 S.-Y. Chiu, H.-W. Huang, T.-H. Huang, K.-C. Liang, K.-P. Liu, J.-H. Tsai and W.-S. Lour, *IEEE Electron Devices Lett.*, 2008, **29**, 1328–1331.
5 T. Mueller, F. Xia and P. Avouris, *Nat. Photonics*, 2010, **4**, 297–301.
6 E. Ponomarev, I. Gutierrez-Lezama, N. Ubrig and A. F. Morpurgo, *Nano Lett.*, 2015, **15**, 8289–8294.
7 A. Avsar, J. Y. Tan, M. Kurpas, M. Gmitra, K. Watanabe, T. Taniguchi, J. Fabian and B. Özyilmaz, *Nat. Phys.*, 2017, **13**, 888–893.
8 F. Wang, L. Li, W. Huang, L. Li, B. Jin, H. Li and T. Zhai, *Adv. Funct. Mater.*, 2018, **28**, 1802707.
9 C.-H. Lee, G.-H. Lee, A. M. van der Zande, W. Chen, Y. Li, M. Han, X. Cui, G. Arefe, C. Nuckolls, T. F. Heinz, J. Guo, J. Hone and P. Kim, *Nat. Nanotechnol.*, 2014, **9**, 676.
10 M. Massicotte, P. Schmidt, F. Vialla, K. G. Schädler, A. Reserbat-Plantey, K. Watanabe, T. Taniguchi, K. J. Tielrooij and F. H. L. Koppens, *Nat. Nanotechnol.*, 2016, **11**, 42–46.
11 W. Luo, Y. Cao, P. Hu, K. Cai, Q. Feng, F. Yan, T. Yan, X. Zhang and K. Wang, *Adv. Opt. Mater.*, 2015, **3**, 1418.
12 X. Wei, F. Yan, Q. Lv, C. Shen and K. Wang, *Nanoscale*, 2017, **9**, 8388–8392.
13 Q. Lv, F. Yan, X. Wei and K. Wang, *Adv. Opt. Mater.*, 2018, **6**, 1700490.
14 Z. Yu, Y. Pan, Y. Shen, Z. Wang, Z. Y. Ong, T. Xu, R. Xin, L. Pan, B. Wang, L. Sun, J. Wang, G. Zhang, Y. W. Zhang, Y. Shi and X. Wang, *Nat. Commun.*, 2014, **5**, 5290.
15 L. Li, Y. Yu, G. J. Ye, Q. Ge, X. Ou, H. Wu, D. Feng, X. H. Chen and Y. Zhang, *Nat. Nanotechnol.*, 2014, **9**, 372–377.
16 X. Yu, P. Yu, D. Wu, B. Singh, Q. Zeng, H. Lin, W. Zhou, J. Lin, K. Suenaga, Z. Liu and Q. J. Wang, *Nat. Commun.*, 2018, **9**, 1545.
17 K. Leng, I. Abdelwahab, I. Verzhbitskiy, M. Telychko, L. Chu, W. Fu, X. Chi, N. Guo, Z. Chen, Z. Chen, C. Zhang, Q. H. Xu, J. Lu, M. Chhowalla, G. Eda and K. P. Loh, *Nat. Mater.*, 2018, **17**, 908–914.
18 J. Wu, H. Yuan, M. Meng, C. Chen, Y. Sun, Z. Chen, W. Dang, C. Tan, Y. Liu, J. Yin, Y. Zhou, S. Huang, H. Q. Xu, Y. Cui, H. Y. Hwang, Z. Liu, Y. Chen, B. Yan and H. Peng, *Nat. Nanotechnol.*, 2017, **12**, 530–534.
19 C. Chen, M. Wang, J. Wu, H. Fu, H. Yang, Z. Tian, T. Tu, H. Peng, Y. Sun, X. Xu, J. Jiang, N. B. M. Schroter, Y. Li, D. Pei, S. Liu, S. A. Ekahana, H. Yuan, J. Xue, G. Li, J. Jia, Z. Liu, B. Yan, H. Peng and Y. Chen, *Sci. Adv.*, 2018, **4**, eaat8355.
20 H. Fu, J. Wu, H. Peng and B. Yan, *Phys. Rev. B: Condens. Matter Mater. Phys.*, 2018, **97**, 241203(R).
21 H. Li, X. Xu, Y. Zhang, R. Gillen, L. Shi and J. Robertson, *Sci. Rep.*, 2018, **8**, 10920.
22 J. Yin, Z. Tan, H. Hong, J. Wu, H. Yuan, Y. Liu, C. Chen, C. Tan, F. Yao, T. Li, Y. Chen, Z. Liu, K. Liu and H. Peng, *Nat. Commun.*, 2018, **9**, 3311.
23 J. Li, Z. Wang, Y. Wen, J. Chu, L. Yin, R. Cheng, L. Lei, P. He, C. Jiang, L. Feng and J. He, *Adv. Funct. Mater.*, 2018, **28**, 1706437.
24 Q. Fu, C. Zhu, X. Zhao, X. Wang, A. Chaturvedi, C. Zhu, X. Wang, Q. Zeng, J. Zhou, F. Liu, B. K. Tay, H. Zhang, S. J. Pennycook and Z. Liu, *Adv. Mater.*, 2019, **31**, 1804945.
25 Y. Liu, J. Guo, E. Zhu, L. Liao, S. J. Lee, M. Ding, I. Shakir, V. Gambin, Y. Huang and X. Duan, *Nature*, 2018, **557**, 696–700.
26 C. Kim, I. Moon, D. Lee, M. S. Choi, F. Ahmed, S. Nam, Y. Cho, H. J. Shin, S. Park and W. J. Yoo, *ACS Nano*, 2017, **11**, 1588–1596.
27 C. Gong, L. Colombo, R. M. Wallace and K. Cho, *Nano Lett.*, 2014, **14**, 1714–1720.
28 Y. Liu, P. Stradins and S. H. Wei, *Sci. Adv.*, 2016, **2**, e1600069.
29 D. He, J. Qiao, L. Zhang, J. Wang, T. Lan, J. Qian, Y. Li, Y. Shi, Y. Chai, W. Lan, L. K. Ono, Y. Qi, J. B. Xu, W. Ji and X. Wang, *Sci. Adv.*, 2017, **3**, e1701186.
30 W. S. Leong, Q. Ji, N. Mao, Y. Han, H. Wang, A. J. Goodman, A. Vignon, C. Su, Y. Guo, P. C. Shen, Z. Gao, D. A. Muller, W. A. Tisdale and J. Kong, *J. Am. Chem. Soc.*, 2018, **140**, 12354–12358.
31 T. Uwanno, Y. Hattori, T. Taniguchi, K. Watanabe and K. Nagashio, *2D Mater.*, 2015, **2**, 041002.
32 J. Wu, C. Tan, Z. Tan, Y. Liu, J. Yin, W. Dang, M. Wang and H. Peng, *Nano Lett.*, 2017, **17**, 3021–3026.

33 A. Allain, J. Kang, K. Banerjee and A. Kis, *Nat. Mater.*, 2015, **14**, 1195–1205.

34 W. Zhang, J. K. Huang, C. H. Chen, Y. H. Chang, Y. J. Cheng and L. J. Li, *Adv. Mater.*, 2013, **25**, 3456–3461.

35 H. Fang and W. Hu, *Adv. Sci.*, 2017, **4**, 1700323.

36 X. Liu, X. Chen, J. Yi, Z. Luo, H. Nan, H. Guo, Z. Ni, Y. Ding, S. Dai and X. Wang, *Org. Electron.*, 2019, **64**, 22–26.

37 G. Konstantatos, M. Badioli, L. Gaudreau, J. Osmond, M. Bernechea, F. P. G. de Arquer, F. Gatti and F. H. L. Koppens, *Nat. Nanotechnol.*, 2012, **7**, 363–368.

38 J. Wang, H. Fang, X. Wang, X. Chen, W. Lu and W. Hu, *Small*, 2017, **13**, 1700894.

39 Y. Cao, K. Cai, P. Hu, L. Zhao, T. Yan, W. Luo, X. Zhang, X. Wu, K. Wang and H. Zheng, *Sci. Rep.*, 2015, **5**, 8130.